Characterization and Correction of Intersensor Calibration Convolution Errors Between S-NPP OMPS Nadir Mapper and Metop-B GOME-2

Ding Liang, Banghua Yan, and Lawrence Flynn

***Abstract*— This article introduces a method to correct intersensor calibration convolution errors that occur in the convolution of spectral response functions (SRFs) between narrow-band and broad-band instruments. By using the intersensor calibration analysis between Ozone Mapping and Profiler Suite (OMPS) Nadir Mapper (NM) and Global Ozone Monitoring Experiment-2 (GOME-2) as an example, the root cause of convolution errors in the intersensor calibration is addressed through direct comparison of OMPS NM SRF and convolved OMPS SRF with GOME-2 SRF. The results reveal that distorted SRF of the narrow-band instrument is the major cause, which appears for GOME-2 at a wide range of channels. The convolution errors in reflectance, which were ignored in previous studies, can be greater than 2% for wavelength shorter than 320 nm and ∼0.5% for wavelengths between 320 and 330 nm. This study thus presents a hybrid convolution error correction method that consists of theoretical approximation of the convolution errors and empirical estimates of residuals due to the deviation of the theoretical approximation from the actual convolution errors. According to the validation through simulation, after applying convolution error correction, the mean convolution errors are less than 0.02%, while the root mean square errors are reduced from more than 0.5% to less than 0.1%. In addition, the correction method is applied to the intersensor calibration radiometric bias assessment between the Meteorological Operational satellite–B (Metop-B) GOME-2 and the Suomi National Polar-orbiting Partnership (S-NPP) OMPS NM. The averaged intersensor calibration reflectance differences are decreased by more than 16% after convolution error correction.**

***Index Terms*— Convolution, GOME-2, intersensor calibration, linear regression, Metop-B, Nadir Mapper (NM), Ozone Mapping and Profiler Suite (OMPS), radiative transfer model, reflectance, Sensor Data Record (SDR), simultaneous nadir overpass, spectral response function (SRF), Suomi National Polar-orbiting Partnership (S-NPP).**

I. Introduction

MEASUREMENT spectral convolutions are widely used in assessing satellite intersensor calibration radiometric biases to mitigating the inconsistency in sensor bandwidth and spectral response function (SRF) [1]–[4]. In order to reduce the impacts from spectral mismatch from intersensor calibration of two instruments with narrow and broad

Manuscript received May 19, 2021; revised October 12, 2021; accepted November 18, 2021. Date of publication December 10, 2021; date of current version March 3, 2022. This work was supported by the JPSS Integrated Calibration and Validation System (ICVS) Project through the JPSS Program. *(Corresponding author: Ding Liang.)*

Ding Liang is with the Center for Satellite Application and Research, Global Science and Technology, College Park, MD 20910 USA (e-mail: ellen.dingliang@gmail.com).

Banghua Yan is with Center for Satellite Applications and Research, NOAA, College Park, MD 20746 USA.

Lawrence Flynn is with NOAA/NESDIS/STAR/SMCD/SPB, NOAA, Washington, DC 20746 USA.

Digital Object Identifier 10.1109/TGRS.2021.3134206

TABLE I
SETTINGS OF GOME-2 BAND 2B AND OMPS/NM

Parameter	GOME-2 Band 2B	OMPS NM
Wavelength range	308-402 *nm*	300-380 *nm*
Spectral Sampling interval	0.12 *nm*	0.42 *nm*
Nadir pixel size	40 x 80 km^2	50 x 50 km^2
Bandwidth	0.28 *nm*	1.0 *nm*

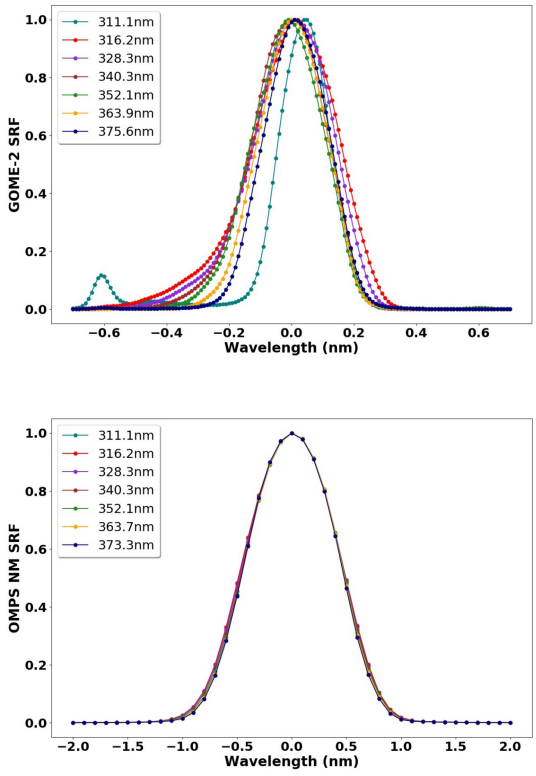

Fig. 1. (Top) Metop-B GOME-2 maximum response normalized SRF for channels, 311.1, 316.2, 328.3, 340.3, 352.1, 363.9, and 375.6 nm. (Bottom) S-NPP OMPS NM maximum response normalized SRF for channels, 311.1, 316.2, 328.3, 340.3, 352.1, 363.7, and 373.3 nm.

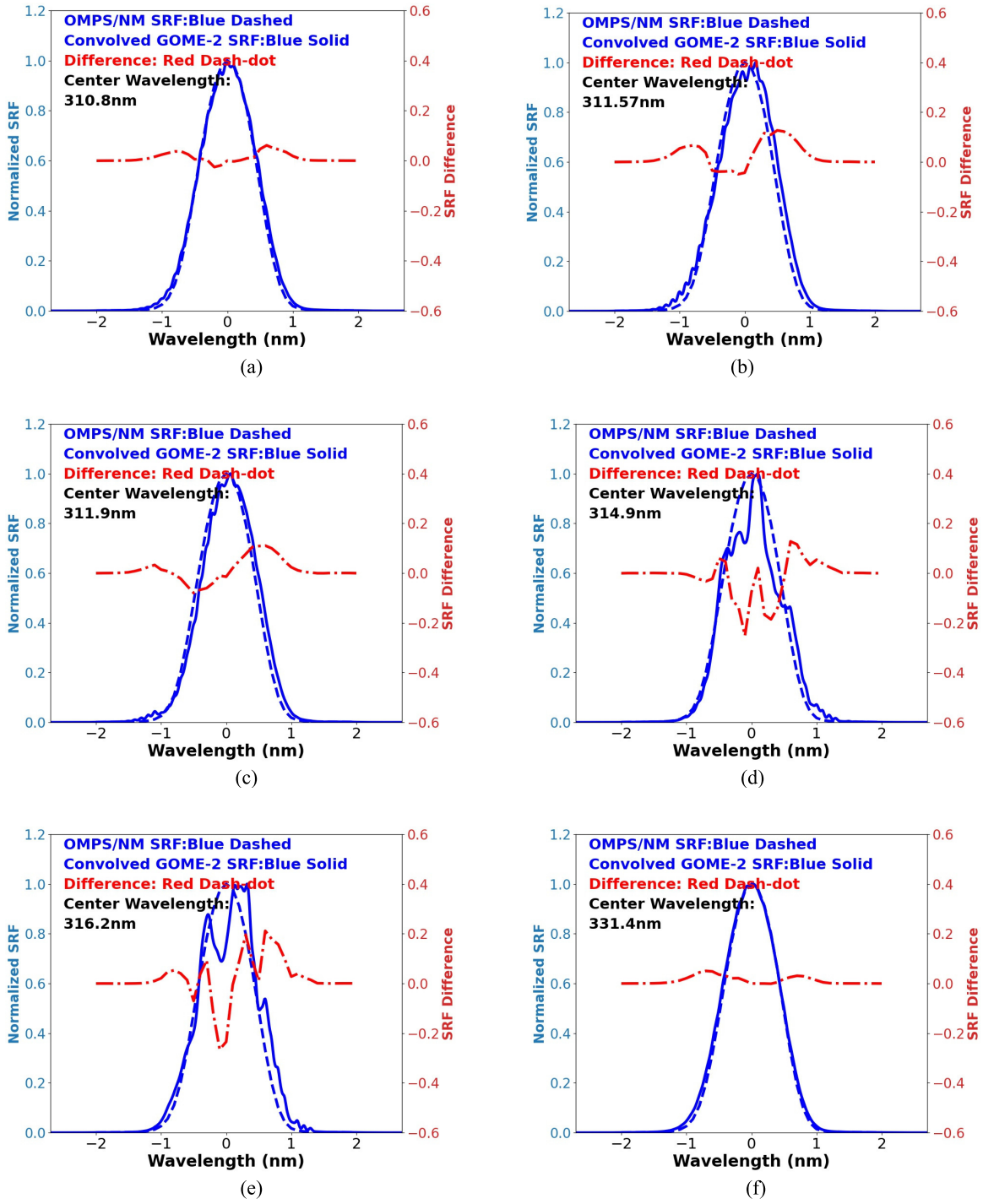

Fig. 2. Maximum response normalized convolved GOME-2 SRF (blue solid line, left coordinate), maximum response normalized OMPS/NM SRF (blue dashed line, left coordinate), and their difference (red dashed-dotted lines, right coordinate) for channels. (a) 310.8 nm. (b) 311.57 nm. (c) 311.9 nm. (d) 314.9 nm. (e) 316.2 nm. (f) 331.4 nm.

bandwidths, one widely used approach is to expand the bandwidth of the narrow-band instrument to that of the broadband instrument by convolving the narrow-band instrument's observation spectrum with the SRF of the broadband instrument [1]. Atmospheric Infrared Sounder (AIRS) spectra are convolved with Moderate resolution Imaging Spectroradiometer (MODIS) SRF before assessing the calibration of MODIS [1]. AIRS spectra are convolved with High-resolution Infrared Radiation Sounder (HIRS) SRF before conducting the intersensor comparison [2]. AIRS and Infrared Atmospheric Sounding Interferometer (IASI) spectra are convolved with the Geosynchronous Operational Environmental Satellite (GOES) imager SRF before comparing AIRS and IASI using GOES imagers as a transfer standard [3]. A Global Ozone Monitoring Experiment-2 (GOME-2) spectrum is convolved with the Ozone Mapping and Profiler Suite (OMPS) Nadir Mapper (NM) SRF before evaluating OMPS NM Sensor Data Record (SDR) data quality [4]. Previous studies show that

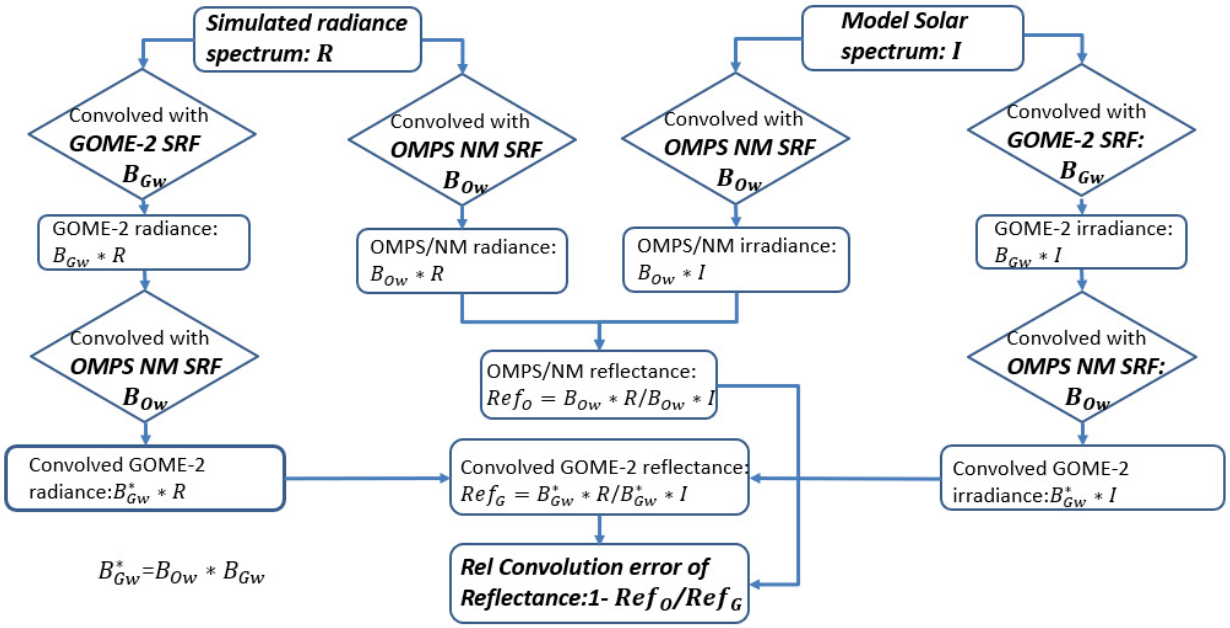

Fig. 3. Schematic for convolution errors in reflectance calculation. Inputs of radiance, model solar spectrum and SRFs, and output of relative convolution errors are highlighted in bold italic style.

convolution errors usually remain in corresponding intersensor calibration error assessments, when the narrow-band instrument has a bandwidth that is not small enough or has a distorted SRF [1], [2], [5], [6]. Convolution errors were considered small and ignorable in some studies [3], [4]; however, they can be significant when compared with the stringent calibration accuracy requirement imposed by future climate missions [5]. In [1] and [2], convolution errors were estimated by average of those computed for each of the standard atmospheres. In reality, convolution errors were found to depend on the atmospheric state, Earth surface, and cloud conditions [1], [2], [5] which resulted in the development of a linear regression method using radiance as indicator [5] to mitigate convolution errors in intersensor calibration between MODIS and infrared sounders. However, this method is not proper for GOME-2 and OMPS NM as their convolution errors are not linear with radiance. According to our analysis, the convolution errors can have significant impacts on the intersensor calibration reflectance difference between OMPS NM and Metop-B GOME-2 if no correction is applied. This calls for algorithm development of convolution error correction for the intersensor comparison between GOME-2 and OMPS NM.

This study first characterizes convolution errors in intersensor comparison between Metop-B GOME-2 and OMPS NM through radiative transfer model simulations. The convolution of SRFs from GOME-2 on board Metop-B and OMPS NM on board Suomi National Polar-orbiting Partnership (S-NPP) is compared with original OMPS NM SRF to show how the shape of GOME-2 SRF impacts the convolved SRF. In the simulations, the convolution error is the difference between the double convolution of model simulated monochromatic spectra with both GOME-2 SRF and OMPS NM SRF and the single convolution of the same spectra with OMPS NM SRF. Explicit expressions of convolution errors are derived in this article. To mitigate convolution errors in intersensor calibration between GOME-2 and OMPS NM, a hybrid convolution error correction method is presented based on estimation of scene convolution errors (major contribution) from explicit equations and estimation of residual scene convolution errors (minor contributor) from an empirical fitting. In this paper, a total of 1223 randomly distributed, clear-sky radiance spectra are simulated using realistic geophysical properties to validate the correction method. These spectra cover a wide range of atmospheric conditions and include both land and ocean scenes. Among these spectra, 723 randomly selected spectra are used to validate the first step of the hybrid correction method and also calculate the residual convolution errors which are used as correction look-up-tables (LUTs). The remaining 500 radiance spectra are used to validate both the first step of the correction method and the residual convolution error correction LUTs.

Furthermore, this hybrid convolution error correction method is applied to life time intersensor calibration differences calculation between S-NPP OMPS NM and GOME-2 Metop-B to evaluate the impact of the convolution error corrections, where the collocated data sets between two satellite instruments are generated based on an existing Simultaneous Nadir Overpass (SNO) method [7].

This article consists of five parts. After this introduction, Section II includes instrument descriptions and describes the process to identify and collect SNO collocated pixel pairs. In Section III, characterization of convolution errors is presented based on simulated monochromatic spectra, along with an explicit form of convolution of SRFs from GOME-2 and OMPS NM. In the fourth part, a hybrid convolution error correction method is introduced and validated using independent radiative transfer model simulations. The hybrid convolution error correction method is further applied to intersensor comparison between Metop-B GOME-2 and S-NPP OMPS NM at their collocated SNO pixels from 2013 to 2020.

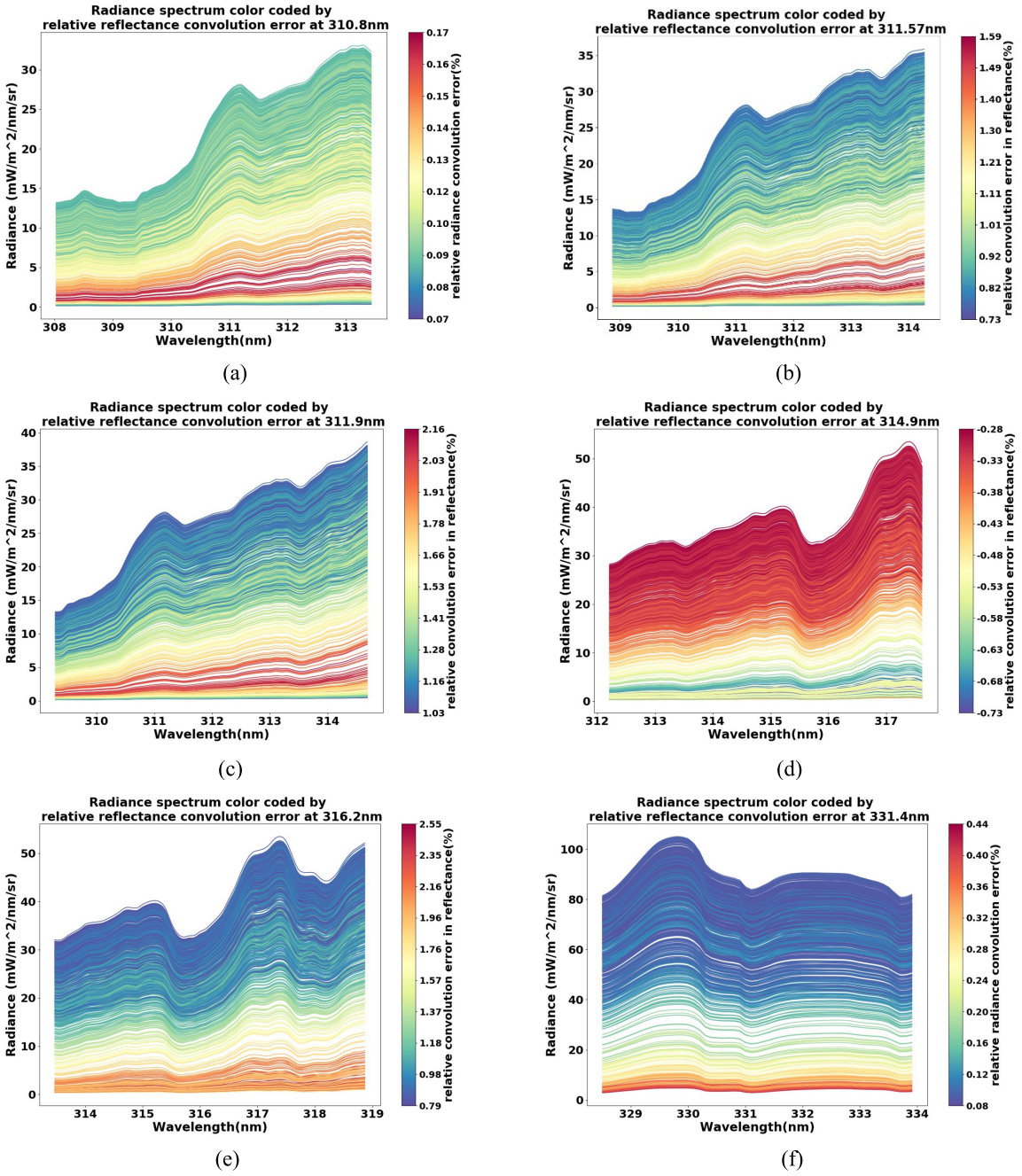

Fig. 4. TOMRad model simulated radiance spectrum color coded by corresponding convolution errors in reflectance calculated from (3B). The radiance spectrum covers ±2.7 nm from center wavelengths of (a) 310.8, (b) 311.57, (c) 311.9, (d) 314.9, (e) 316.2, and (f) 331.4 nm.

The final part summarizes the results and conclusions. Unless otherwise stated, convolution errors in this paper represent relative convolution errors in reflectance.

II. Instruments Description and SNO Pixel Pairs Collection

A. . OMPS NM and GOME-2 Instrument Description

The OMPS nadir system consists of a wide field (110°) telescope and two spectrometers: An NM covering 300 to 380 nm in 196 channels with a 50-km nadir footprint for mapping total column ozone across a 2800 km swath with 35 footprints totally, and a Nadir Profiler covering 250 to 310 nm with a single 250-km footprint to provide ozone profile information [4], [8]–[10]. The S-NPP NM is examined in this article, where the spectral resolution is approximately 1.0 nm for most wavelengths and the spectral sampling interval is approximately 0.42 nm [4], [8]–[10]. Since S-NPP was launched in October 2011, a second OMPS NM instrument was carried on board the NOAA20 satellite which was launched in November 2017. In the future, OMPS NM instruments will be onboard three more Joint Polar-orbiting satellite system (JPSS) polar-orbiting satellites. GOME-2 has been carried on Metop-A, -B, and -C. GOME-2 on board Metop-B was launched in September 2012. It covers wavelengths from 239 to 791 nm

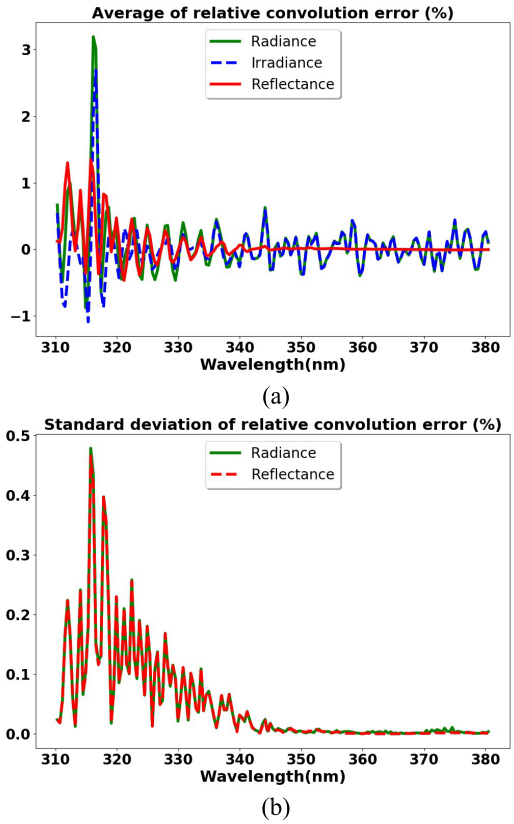

Fig. 5. (a) Green: averaged convolution errors in radiance calculated using 723 cases of simulated radiance from (3A). Red: averaged convolution errors in reflectance calculated using 723 cases of simulated radiance from (3B). Blue: convolution errors in solar irradiance calculated using single solar spectrum from (3A). (b) Green: standard deviation of convolution errors in radiance calculated using 723 cases of simulated radiance. Red: standard deviation of convolution errors in reflectance calculated using 723 cases of simulated radiance.

in four main science channels named channels 1–4 [11]. Channel 2 has two bands: band 2A and band 2B. Band 2B of channel 2 which covers approximately 308 to 402 nm is used in this article. This band includes 953 wavelengths with a spectral sampling interval of 0.12 nm. The spectral resolution is approximately 0.28 nm for most wavelengths. The ground pixel size (across track × along track) is 80 × 40 km^2. The instrument is operated to make 24 forward viewing cross-track scan integrations where the 12th and 13th are close to nadir within 3° of zenith view angles. The scene on the west side of the track is used in this study since it has smaller viewing zenith angle. The OMPS NM and GOME-2 instrument specifications are briefed in Table I.

Fig. 1 shows discrete SRFs at selected channels for Metop-B GOME-2 and S-NPP OMPS NM. S-NPP OMPS NM has symmetric bell-shaped SRFs that do not change much between channels. However, the SRFs for Metop-B GOME-2 vary with wavelengths and the short wavelength channels have obviously distorted SRFs. It will be shown later in Section 3 that the distorted SRF is the major cause of convolution errors.

B. SNO Collocated Pixel Pairs Screening

Intersatellite calibration through satellites SNO pixel pairs has been widely used since the SNO method was first introduced in 2002 by Cao *et al.* [7], [12], [13]. Uprety *et al.* [14] estimated radiometric bias between S-NPP/Visible Infrared Imaging Radiometer Suite (VIIRS) and Aqua/MODIS using their low-latitude SNOs. Cao *et al.* assessed radiometric consistency among VIIRS, MODIS, and advanced very high-resolution radiometer (AVHRR) using their SNOs [15]. SNO events between S-NPP and Metop-B have a recurrence cycle of about 50 days and each time lasts for 2–3 days. They are present at latitude between 70° and 75° and in both the north and south polar regions [4]. The near real-time SNO occurrence information can be found from NOAA National Calibration Center (NCC) (https://ncc.nesdis.noaa.gov/SNOPredictions/index.php) [12], [13]. The SNO pixel pairs used in this study are obtained by comparing pixels center geolocation distance and observation time difference from GOME-2 level 1 B data and OMPS NM SDR data.

The following quality control (QC) criteria are used to screen out collocated clear-sky pixel pairs: 1) pixel pair spatial distances are less than 30 km to ensure that the Metop-B GOME-2 pixel is within in the cluster formed by S-NPP OMPS NM nadir pixel and surrounding eight pixels; 2) the standard deviation of reflectance from the nine pixels in the cluster is within 2% of their mean; 3) OMPS NM reflectances at 331 nm are less than 0.3 so that they are clear or close to clear-sky pixels [9]; 4) the temporal difference is set to less than 120 s to make sure the change of atmospheric status in the observation path is small enough and does not significantly impact satellite observations; and 5) solar zenith angles are restricted to less than 70° to exclude highly noisy S-NPP OMPS NM observations. An assumption is made that collocated GOME-2 and NM pixels that satisfy criteria [1] and [2] have homogeneous backgrounds. Approximately ten collocated pixel pairs are found in the 2–3 days period for most SNO events between October 2012 and August 2020 in the Northern hemisphere. There are no collocated pixel pairs found in winter in the North hemisphere due to lack of day time observations at high latitude where the SNO happens.

III. Characterization of Convolution Errors Between GOME-2 and OMPS NM

A. Formula for Convolution Error Calculation

GOME-2 and OMPS NM measurements can be written as convolution of SRF and illumination to the satellite sensors

$$Y_G(w) = B_{Gw} * X = \sum_{k=-70}^{70} B_{Gw}(k\Delta_G)X(w + k\Delta_G) \quad (1A)$$

$$Y_O(w) = B_{Ow} * X = \sum_{n=-20}^{20} B_{Ow}(n\Delta_O)X(w + n\Delta_O) \quad (1B)$$

where $*$ is the convolution symbol and it also represents the summation of discrete illumination weighted by discrete SRF; $Y(w)$ is radiance or solar irradiance measured at wavelength w; the subscripts G or O refer to GOME-2 and OMPS NM, respectively; B_{Gw} and B_{Ow} are normalized GOME-2 and OMPS NM SRF centered at wavelength w; B_{Gw} has sampling interval of $\Delta_G = 0.01$ nm for GOME-2 band 2B and

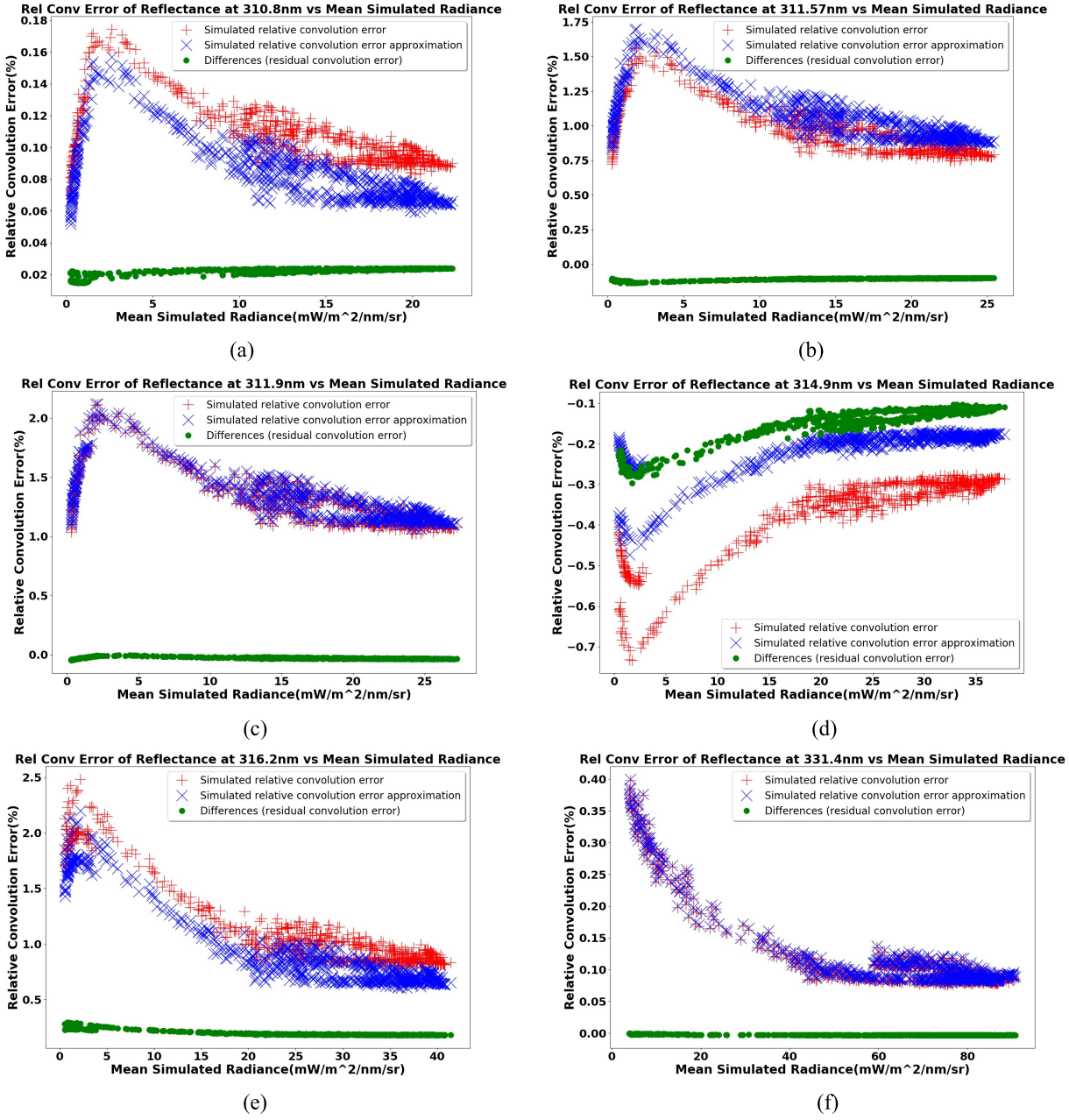

Fig. 6. Scattered plots of convolution errors calculated from 723 simulated radiance spectrum for channels. (a) 310.8 nm. (b) 311.57 nm. (c) 311.9 nm. (d) 314.9 nm. (e) 316.2 nm. (f) 331.4 nm versus mean of simulated radiance spectrum between center wavelengths ±2.7 nm. Red +: Convolution error is calculated from (4B); blue X: convolution error is approximated using (5); green: difference between red + and blue X, that is, residual convolution error calculated from (6).

covers ±0.7 nm from the center wavelength; and B_{Ow} covers ±2 nm from the center wavelength with a sampling interval of $\Delta_O = 0.1$ nm. X is radiance or solar irradiance illumination. X has an infinite spectral resolution, where each channel of radiance or irradiance from X is monochromatic with a zero bandwidth. Convolution of GOME-2 measurements with OMPS NM SRF takes the form

$$Y_G^*(w) = B_{Ow} * Y_G = B_{Ow} * B_{Gw} * X \tag{2}$$

where $Y_G^*(w)$ represents convolved GOME-2 radiance or irradiance measured at wavelength w.

Technically, the convolution errors in radiance or irradiance at wavelength w are defined as the difference between convolved GOME-2 measurements $Y_G^*(w)$ and OMPS NM measurements $Y_O(w)$ divided by convolved GOME-2 measurements $Y_G^*(w)$

$$\delta_X(w) = \frac{Y_G^*(w) - Y_O(w)}{Y_G^*(w)} = \frac{B_{Ow} * B_{Gw} * X - B_{Ow} * X}{B_{Ow} * B_{Gw} * X}. \tag{3A}$$

The convolution errors in reflectance at wavelength w also takes the form

$$\delta_R(w) = \frac{B_{Ow} * B_{Gw} * R/(B_{Ow} * B_{Gw} * I) - B_{Ow} * R/(B_{Ow} * I)}{B_{Ow} * B_{Gw} * R/(B_{Ow} * B_{Gw} * I)}. \tag{3B}$$

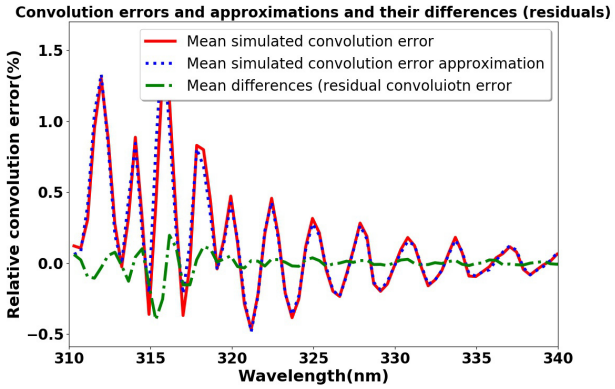

Fig. 7. Red solid line: average of simulated convolution errors from red + in Fig. 6. Blue dots: average of simulated convolution error approximation from blue X in Fig. 6. Green dashed-dotted line: average of difference between them, that is, average of green dots in Fig. 6. These are also the values assigned for the residual correction LUT.

where R and I without subscript are monochromatic radiance and solar irradiance illumination, respectively. Equations (3A) and (3B) show that, if GOME-2 has infinite spectral resolution, that is, if B_{Gw} is an impulse function which equals 1 at center wavelength and equals 0 everywhere else [17], then $B_{Ow} * B_{Gw} * X$ in (3A) and (3B) would equal to $B_{Ow} * X$, which would result in zero convolution error. In practice, however, the above assumption is invalid, and thus nonzero convolution errors are present.

Equations (3A) and (3B) can also be written as the following forms:

$$\begin{aligned}\delta_X(w) &= \frac{B^*_{Gw} * X B_{Ow} * X}{B^*_{Gw} * X} \\ &= \frac{\left(B^*_{Gw} - B_{Ow}\right) * X}{B^*_{Gw} * X} \\ &= 1 - \frac{B_{Ow} * X}{B^*_{Gw} * X} \end{aligned} \tag{4A}$$

$$\begin{aligned}\delta_R(w) &= \frac{B^*_{Gw} * R/\left(B^*_{Gw} * I\right) - B_{Ow} * R/(B_{Ow} * I)}{B^*_{Gw} * R/\left(B^*_{Gw} * I\right)} \\ &= 1 - \frac{B_{Ow} * R/(B_{Ow} * I)}{B^*_{Gw} * R/\left(B^*_{Gw} * I\right)} \end{aligned} \tag{4B}$$

where convolved GOME-2 SRF is defined as: $B^*_{Gw} = B_{Ow} * B_{Gw}$. B^*_{Gw} covers ±2.7 nm from the center wavelength with the sampling interval equal to the smaller sampling interval of the two sensors, that is, 0.01 nm. Appendix A shows weighted summation form of B^*_{Gw}, $\delta_X(w)$, and $\delta_R(w)$.

B. Root Cause and Characterization of Convolution Errors for NM and GOME-2

The root cause of the convolution errors can be addressed via (4A) and (4B). Equations (4A) and (4B) show that convolution errors depend on OMPS SRF (B_{Ow}), convolved GOME-2 SRF (B^*_{Gw}), monochromatic radiance, and solar irradiance spectrum. Particularly, as shown in (4A), the difference between convolved B^*_{Gw} and B_{Ow} plays a key role in convolution errors. Normalized SRFs B^*_{Gw} and B_{Ow} for selected wavelength are compared in Fig. 2. These two SRFs do not agree well with each other: at 311.57, 314.9, and 316.2 nm, the convolved GOME-2 SRFs are distorted; at 311.9 nm, although the shape of convolved GOME-2 SRFs is not as distorted as other channels, there is a shift in the wavelength direction between it and the OMPS NM SRF; 331.4 nm has the best agreement in SRFs among all the channels in Fig. 2. The convolved GOME-2 SRFs are distorted to different extent caused by the skewed shape of GOME-2 SRF especially at shorter wavelength channels which can be seen from Fig. 1. Convolved GOME-2 SRFs B^*_{Gw} agree better with OMPS NM SRF for wavelength greater than 330 nm, as shown in Fig. 2(f), as GOME-2 SRFs are better shaped at longer wavelength channels. The disagreement between B^*_{Gw} and B_{Ow} will introduce greater convolution errors in measurements at wavelength shorter than 330 nm compared to other channels.

To further understand the relation between convolution errors and radiance inputs and SRFs, 723 cases of backscattered UV radiance spectrum from 300 to 390 nm are simulated using radiative transfer model named TOMRad and a model solar spectrum [10], [18] and then used in (4A) and (4B) to calculate relative convolution errors. Fig. 3 shows the schematic for simulating convolution errors in reflectance using simulated radiance and solar irradiance from (4B).

Fig. 4 shows the 723 simulated radiance spectra for different center wavelengths, where each radiance spectrum curve covers ±2.7 nm from its center wavelength with a color corresponding to the magnitude of convolution errors in reflectance calculated from (4B) (see the color bar). A few finds are summarized from Fig. 4.

First, the convolution errors depend on wavelength: channel 316.2 nm has the highest values which can be as large as 2.5% and channel 310.8 nm has the lowest values which are less than 0.7%. This is because of the large difference between convolved GOME-2 SRF and OMPS NM SRF at 316.2 nm and the small difference between them at 310.8 nm, as shown in Fig. 2.

Second, the convolution errors change with radiance for a given channel: For channels 310.8, 311.57, 311.9, and 314.9 nm, in general, convolution errors increase at first and then decrease as mean radiance increases. For channels 316.2 and 331.4 nm, in general, convolution errors decrease as mean radiance increases.

Last but not least, convolution errors are negative for channel 314.9 nm and positive for other channels, and this result is related to the sign of the integrated differences over the SRF range. As shown in Fig. 2(d), the convolved GOME-2 SRFs are larger than OMPS SRFs when the wavelengths are between 315.4 and 316.2 nm where a radiance valley appears according to Fig. 4(d). In contrast, when convolved GOME-2 SRFs are smaller than OMPS SRFs between 314.5 and 315.4 nm, this region happened to be a radiance peak. This makes the summation of radiance weighted by convolved GOME-2 SRFs smaller than summation of radiance weighted by OMPS SRFs, which leads to negative convolution errors for channel 314.9 nm.

Furthermore, Fig. 5(a) displays the averaged convolution errors in radiance, reflectance, and solar irradiance

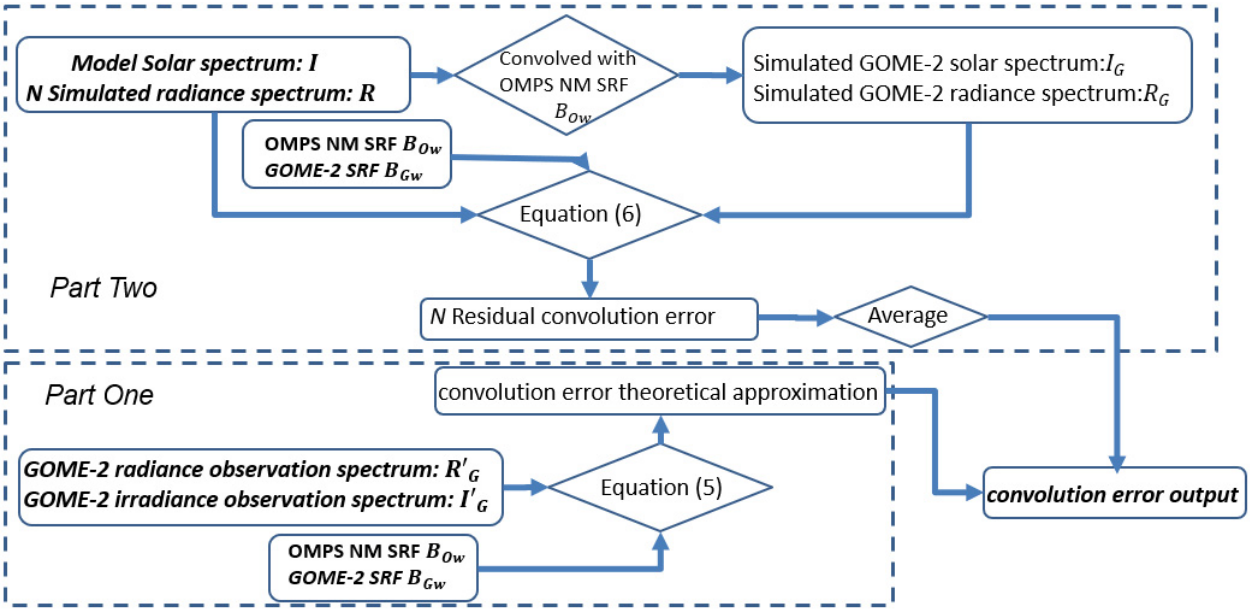

Fig. 8. Schematic for hybrid correction algorithm for convolution errors in reflectance. Inputs of radiance, solar irradiance and SRFs as well as output of convolution errors are highlighted in bold, italic style. The index N in part two denotes the number of simulated cases of residual convolution errors for the LUT calculation and it equals 723 in this article.

versus wavelength. Here, the averaged convolution errors in radiance and reflectance are the averages of those calculated from the 723 simulated radiance spectra. The convolution errors in solar irradiance are calculated from a single solar spectrum. The convolution errors in radiance and solar irradiance have similar amplitude. They reach their maximum value near 316 nm, as explained above. In addition, the averaged convolution errors in reflectance are much smaller than those of radiance and solar irradiance but can still be as large as 1.5% near 316 nm. Fig. 5(b) shows the standard deviation of convolution errors in radiance and reflectance versus wavelength. They are less than 0.3% for most channels. It also shows that when wavelengths are greater than 340 nm, the mean convolution errors in reflectance are very small with the mean value up to 0.1% and standard deviation up to 0.05%.

The convolution errors are important for most of the channels between GOME-2 and OMPS, although the impact is small at the wavelengths above 340 nm. Thus, in Section IV, a convolution error correction method is developed.

IV. Convolution Error Correction Algorithm Development and Application

A. Convolution Error Correction Algorithm

As show by the flowchart in Fig. 3, convolution errors depend on GOME-2 SRF, OMPS NM SRF, monochromatic scene radiance illumination, and scene solar irradiance. The latter two terms are usually unknown in real observations; in this article, they are approximated by observations of radiance and solar irradiance from narrow-band instrument of GOME-2. Thus, a theoretical approximation of the convolution errors can be obtained by using GOME-2 observations of radiance and solar irradiance in place of monochromatic illumination of R and I in (4b). This approximation can be written as

$$\begin{aligned}\delta'_R(w) &= \frac{B^*_{Gw} * R'_G/\left(B^*_{Gw} * I'_G\right) - B_{Ow} * R'_G/\left(B_{Ow} * I'_G\right)}{B^*_{Gw} * R'_G/\left(B^*_{Gw} * I'_G\right)} \\ &= \frac{B^*_{Gw} * R_G/\left(B^*_{Gw} * I_G\right) B_{Ow} * R_G/(B_{Ow} * I_G)}{B^*_{Gw} * R_G/\left(B^*_{Gw} * I_G\right)} \\ &= 1 - \frac{B_{Ow} * R_G/(B_{Ow} * I_G)}{B^*_{Gw} * R_G/\left(B^*_{Gw} * I_G\right)} \end{aligned} \quad (5)$$

where R'_G and I'_G are GOME-2 observations of radiance and solar irradiance with calibration bias; R_G and I_G are bias-free GOME-2 observations of radiance and solar irradiance which equals GOME-2 SRF convolved with monochromatic illumination. Biases in R'_G and I'_G can be canceled out in (5) as they appear in both numerator and denominator, so the bias-free form can also be used.

Differences between (4b) and (5) are the residual convolution errors given in the following equation:

$$\begin{aligned}\delta_R(w) - \delta'_R(w) = &\frac{B_{Ow} * R_G/(B_{Ow} * I_G)}{B^*_{Gw} * R_G/\left(B^*_{Gw} * I_G\right)} \\ &- \frac{B_{Ow} * R/(B_{Ow} * I)}{B^*_{Gw} * R/\left(B^*_{Gw} * I\right)}. \end{aligned} \quad (6)$$

Equations (4b) and (5) are further utilized to calculate convolution errors by using 723 RT model simulated radiance, which represent theoretical and theoretical approximations of convolution errors, respectively. Fig. 6 shows the results of those convolution errors and their differences for center wavelength w at 310.8, 311.57, 311.9, 314.9, 316.1, and 331.4 nm. Generally, the convolution error approximations from (5) agree with the original convolution errors from (4b), with a small amount of differences at some channels. This is particularly true for the wavelengths of 311.9 and

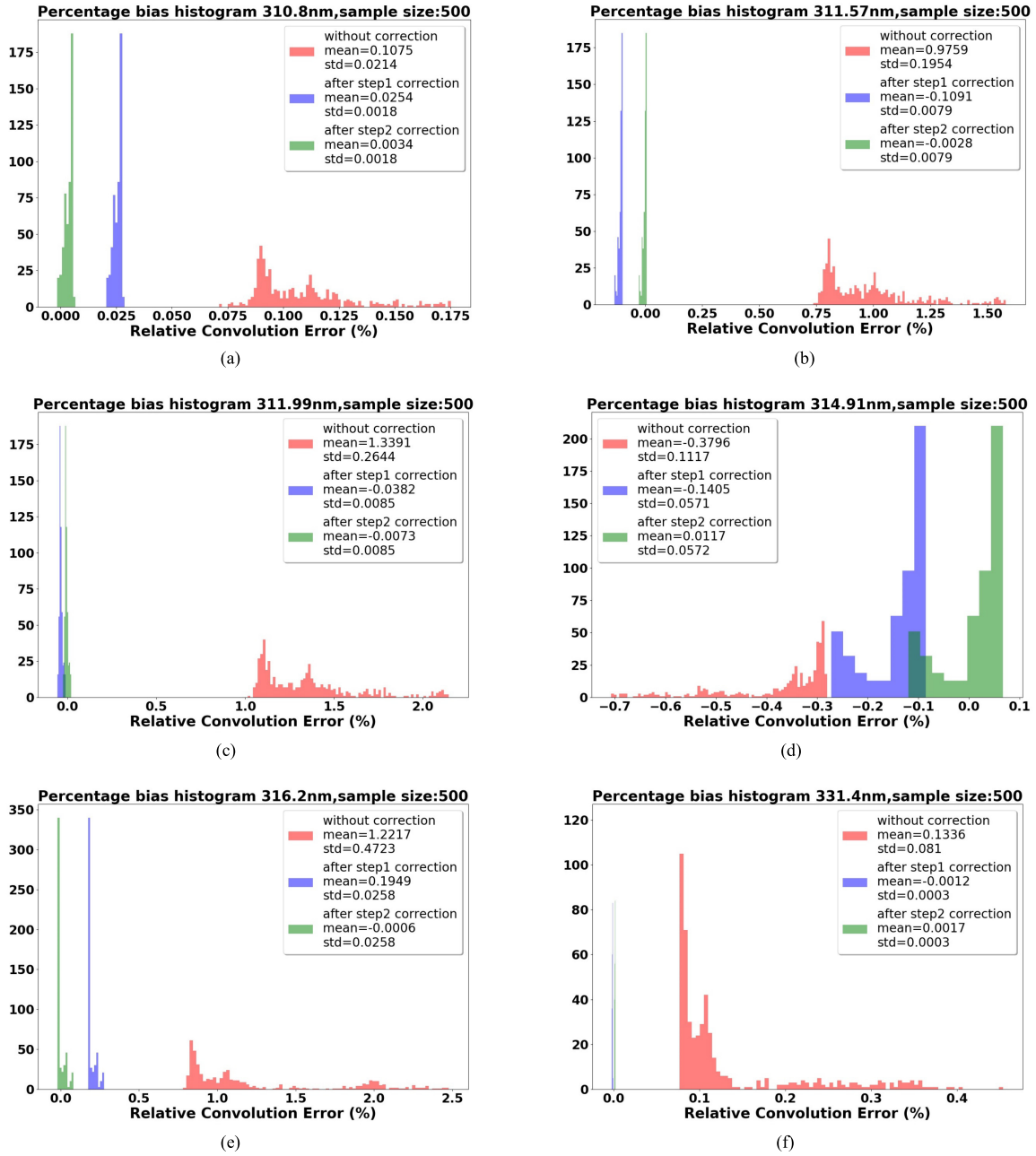

Fig. 9. Histogram of convolution errors before correction, after correcting the theoretical approximation (step 1 correction) and after further correcting the empirical approximation (step 2 correction) for channels. (a) 310.8 nm. (b) 311.57 nm. (c) 311.9 nm. (d) 314.9 nm. (e) 316.2 nm. (f) 331.4 nm.

331.4 nm where the differences are close to 0. However, the difference can be large for some wavelengths. For example, at the wavelength of 316.2 nm, the difference is around 0.25% of reflectance. At the wavelength of 314.9 nm, their difference is around 0.3% of reflectance. Besides, variations of residual convolution errors are very small, which makes estimation of them much easier. Average of the simulated convolution error, simulated convolution error approximation, and residual convolution errors in Fig. 6 is further shown in Fig. 7 for channels from 310 to 340 nm.

Therefore, in this study, the hybrid convolution error correction method consists of two parts of the correction. The first part is the convolution error (major error) correction according to the theoretical approximation calculated by (5) from real time GOME-2 observations of R'_G and I'_G. The second part is the correction of residual convolution errors (minor error) after the first correction is applied. The residuals are corrected by using a LUT which is calculated from the average of simulated cases from (6). Fig. 7 provides averages of simulated convolution errors, convolution error approximations, and residual convolution errors for channels from 310 to 340 nm.

Fig. 8 shows the schematic for this hybrid correction method, where N in part two is the number of simulated cases of residual convolution errors for the LUT calculation. In this

study, N equals 723 as the mean value of residuals shown in Fig. 6 by green dots is used for the LUT, that is, the green dashed-dotted line in Fig. 7 shows the value for this LUT. The theoretical approximation in part one is scene-dependent and channel-dependent. The residual convolution error correction LUT in part two is channel-dependent. The performance of this method is validated in the next section.

B. Algorithm Validation Using Simulations

The performance of the theoretical correction in part one has been well demonstrated by the simulated results in Fig. 6. In this section, we further validate the theoretical correction and also validate the performance of the residual convolution error correction LUT using 500 additional model simulated monochromatic radiance spectra.

Fig. 9 shows the histogram of convolution errors calculated from these additional 500 simulations, difference between convolution errors and their theoretical approximations (step one correction), and difference between convolution errors and summation of their theoretical approximations and residual convolution error correction LUT. The number of bins used is 80 for the histograms before correction and eight for the histograms after correction. Both mean value and standard deviation of convolution errors are greatly reduced after removal of theoretical approximation. The mean values of convolution errors are further reduced after removal of the residual LUT. Mean and standard deviation of convolution errors before and after correction are calculated from all 500 test cases and are shown in Fig. 10 as functions of wavelengths. Fig. 10(a) shows that after removal of theoretical approximations, mean convolution errors are reduced from up to 1.5% to up to 0.25% for channels with positive convolution errors and from up to −0.4% to up to −0.15% for channels with negative convolution errors, except for channels at 315.3 and 317.4 nm. Fig. 10(a) also shows that mean convolution errors have been further reduced to near 0 for all channels after removal of both theoretical approximation and residual correction LUTs. Fig. 10(b) shows that after removal of theoretical approximations, the standard deviations of convolution errors are reduced from values as large as 0.55% down to values smaller than 0.08%. Removal of residual correction LUT does not impact the standard deviation since the LUT is a constant for each channel.

The theoretical approximations in this hybrid convolution error correction algorithm can effectively capture variations in convolution errors by approximating scene convolution errors. Residual convolution errors, which are the difference between the convolution errors and their theoretical approximations, show much less scene dependence and can be effectively corrected by mean residual convolution errors from the simulation results. This two-step convolution error correction method can produce highly accurate results as validated using 500 additional simulations.

C. Application to Metop-B GOME-2 and S-NPP OMPS NM Intersensor Comparison

Previous studies assessed intersensor calibration radiometric biases between Metop-B GOME-2 and S-NPP OMPS NM,

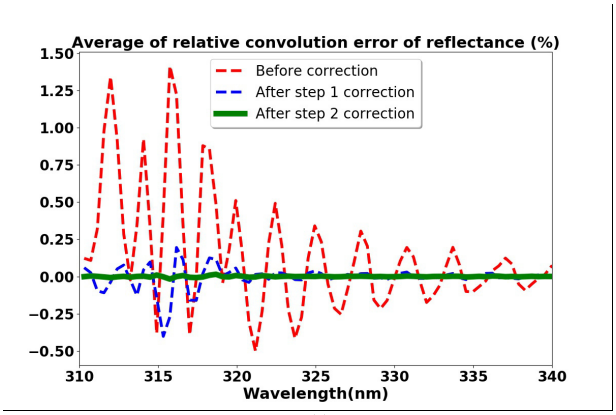

(a)

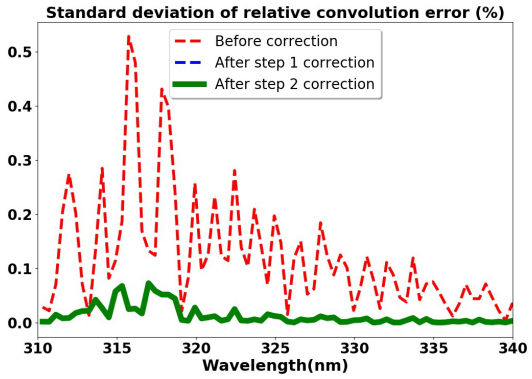

(b)

Fig. 10. (a) Red: averaged convolution errors calculated using 500 cases of simulated radiance. Blue: averaged convolution errors after step 1 correction calculated using 500 cases of simulated radiance. Green: averaged convolution errors after further correction by step 2 method calculated using 500 different cases of simulated radiance. (b) Red: standard deviation of convolution errors before correction calculated using 500 cases of simulated radiance. Green: standard deviation of convolution errors after correction (step 1 + step 2) calculated using 500 cases of simulated radiance.

without the correction of the convolution errors [5], [6]. In the following analysis, we investigate the impact of correcting the convolution errors in improving the intersensor calibration radiometric bias estimates between two sensors. The convolution errors are calculated using the hybrid method as shown in Fig. 8. The collocated data sets between OMPS NM and GOMES-2 are generated using the SNO approach using QC criteria introduced in Section II-B.

We display time series of mean percentage difference between convolved Metop-B/GOME-2 reflectance and S-NPP/NM reflectance at selected channels from June 2013 to August 2020, as given in Fig. 11. Green dots and red dots are the percentage difference of reflectance before and after convolution error correction, respectively. Linear regression fitting lines are also shown in Fig. 11. Due to instrument performance degradation, the percentage difference steadily increased with time and short wavelength channels increased faster than longer wavelength channels. Instrument degradation was found from both GOME-2 Metop-B UV measurements [10], [19], [20] and S-NPP OMPS NM solar measurement [21]. It was predicted that relative reflectance of GOME-2 Metop-B at 325 nm would increase 15% after 7

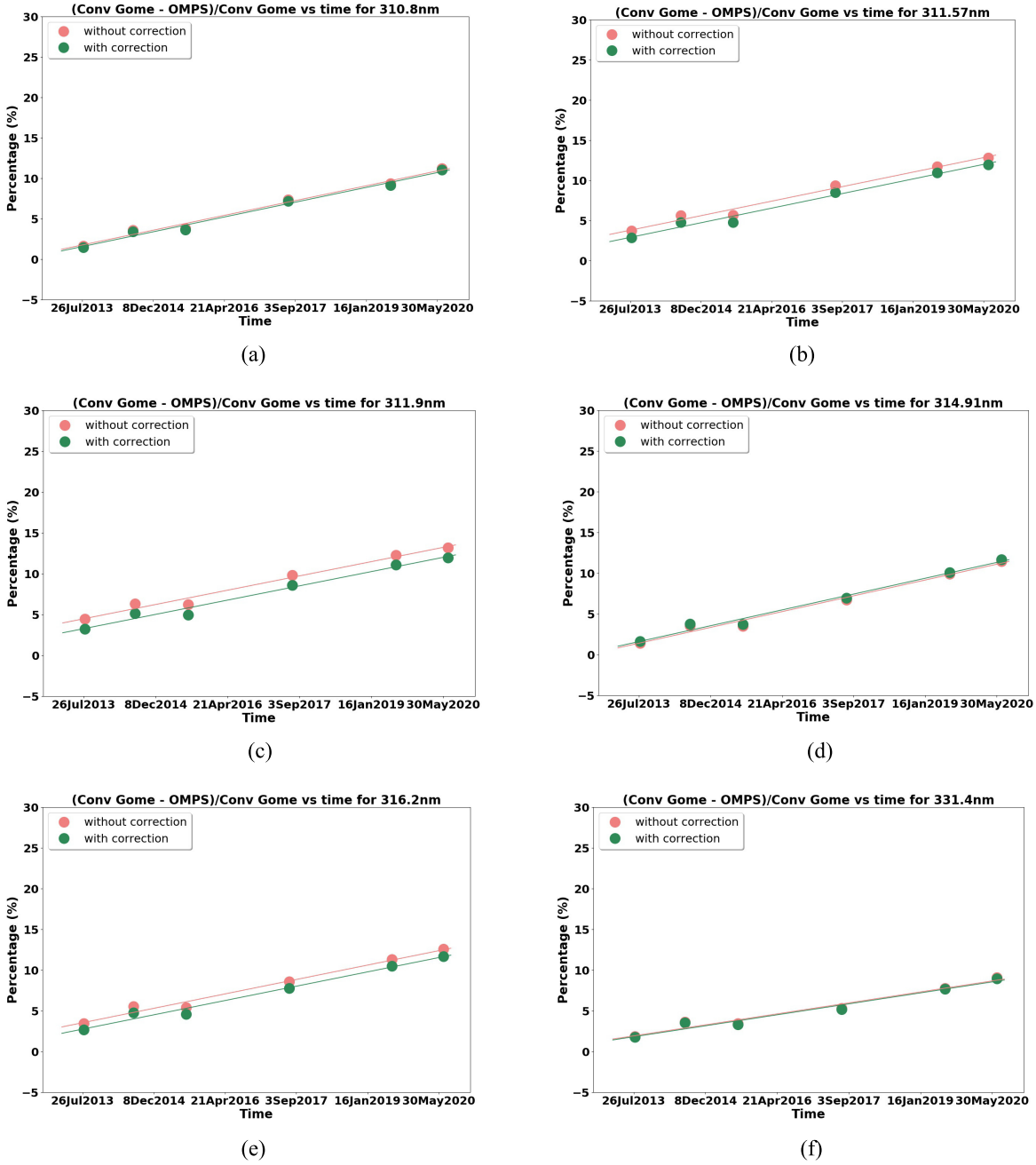

Fig. 11. Time series of mean percentage difference between convolved Metop-B/GOME-2 reflectance and S-NPP/NM reflectance from Jun 2012 to Aug 2020 under clear-sky conditions for channels. (a) 310.8 nm. (b) 311.57 nm. (c) 311.9 nm. (d) 314.9 nm. (e) 316.2 nm. (f) 331.4 nm. Mean percentage difference before convolution error correction and after correction are marked in green and red respectively.

years of operation using Metop-A degradation model and the shorter wavelength channels have higher increase rates [10]. On the other hand, S-NPP OMPS NM optical system degradation is within 0.3% after three and half years of operation [21]. The much larger GOME-2 instrument degradation compared to OMPS /NM is responsible for most of the increase of intersensor comparison percentage difference with time. Despite the above increases caused by instrument degradation, the results have demonstrated the impacts on long time intersensor comparison from convolution error correction: at 311.9 nm, the absolute value of reflectance percentage difference decreased 1.22% on average, that is, a 27.3% to 9.2% change in reflectance difference since they are from less than 5% to over 13% depends on time.

To better understand the contribution of the convolution errors at a given channel, in Fig. 12, we furthermore calculate the percentage of convolution errors in convolved GOME-2 reflectance and percentage of convolution errors in intersensor comparison reflectance difference using all seven years of SNO comparison cases from Fig. 11. The results indicate that one channel at 311.9 nm has mean convolution errors greater than 1.2% of reflectance and greater than 16% of intersensor

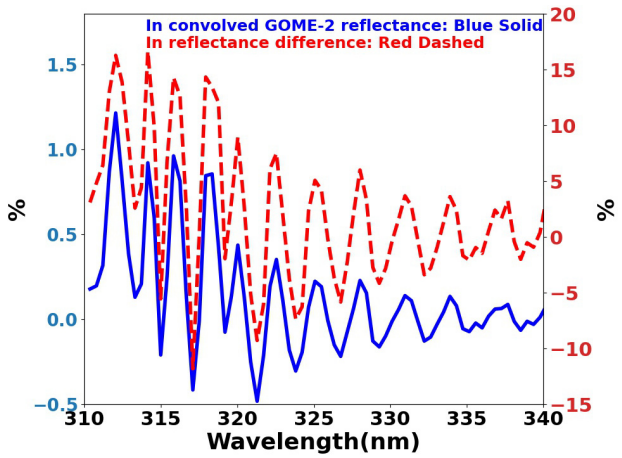

Fig. 12. Convolution errors in reflectance (blue, left coordinate) and in intersensor comparison reflectance difference (red, right coordinate) averaged from all clear-sky SNO comparison cases between Jun 2013 and Aug 2020.

comparison reflectance difference and ten channels with wavelengths between 311 nm and 319 have mean convolution errors greater than 10% of intersensor comparison reflectance difference. Convolution errors are both channel- and scene-dependent. They cannot be removed through averaging the intersensor comparison difference and should be removed by specific algorithms.

The hybrid convolution error correction algorithm has demonstrated its good performance through validation using 500 simulated datasets. In addition, by applying the new algorithm to S-NPP OMPS NM and Metop-B GOME-2 comparison, their averaged intersensor calibration reflectance difference has improved by up to 17% depending on wavelength.

V. Conclusion

This study improves our understanding of the convolution error characterizations in the intersensor calibration bias assessments for two satellite instruments with narrow and broad bandwidths, respectively. First, a formula of SRF for the convolved narrow-band instrument measurements is derived for the first time to facilitate the analysis of the root cause of convolution errors. For Metop-B GOME-2 and S-NPP OMPS NM, significant differences appear between the SRF of convolved GOME-2 measurements and OMPS NM SRF at short wavelength channels less than 330 nm. The big differences are caused by distorted shapes of GOME-2 SRFs leading to relatively large convolution errors between these two instruments at short wavelength channels.

In addition, the convolution error calculation formula and the convolution error correction algorithm are further developed. The convolution errors depend on SRFs from OMPS NM and GOME-2 and monochromatic scene radiance and solar irradiance. Using 723 cases of radiative transfer model simulated monochromatic radiance spectrum, the relative convolution errors in reflectance, radiance, and solar irradiance are simulated. Simulation shows that relative convolution errors in reflectance are not as significant as those of radiance or solar irradiance but can still be higher than 2% at short wavelength channels for individual cases. By using GOME-2 observations of radiance and solar irradiance in place of monochromatic scene radiance and solar irradiance in the convolution error equation, one can get a theoretical approximation of convolution errors. Simulation shows that after removing this theoretical approximation, the convolution errors can be reduced to less than 0.4%. The residual convolution errors show much less dependence on input radiance; thus, mean residual convolution errors from these simulations using 723 datasets are used as empirical approximation to correct the residual convolution errors. This hybrid convolution error correction method is further validated using 500 new cases of radiative transfer model simulations. The reflectance convolution errors can be reduced to less than 0.02% after correcting both theoretical approximation of convolution errors and empirical approximation of residuals.

The convolution error correction method is finally applied to intersensor comparison between OMPS NM on board S-NPP and GOME-2 on board Metop-B at their North hemisphere collocated SNO pixels from 2013 to 2020. The averaged convolution errors in OMPS NM and GOME-2 intersensor comparison reflectance difference range from 17% to −12% depending on the wavelength, demonstrating the impact of the new algorithm in improving the intersensor calibration bias assessment.

The method in this paper can also be applied to intersensor comparison between other instruments. The explicit form of convolution of two instruments' SRF is also derived in Appendix B for general cases and can be used to analyze convolution errors for other instruments with any sampling intervals.

Appendix A
Convolution Error Calculation Formula Derivation

By inserting (A1) into the (2), we get

$$\begin{aligned} Y_G^*(w) &= B_{Ow} * B_G * X \\ &= \sum_{n=-20}^{20} B_{Ow}(n\Delta_O) \sum_{k=-70}^{70} B_{G(w+n\Delta_O)}(k\Delta_G) \\ &\quad \times X(w + n\Delta_O + k\Delta_G). \end{aligned} \tag{A1}$$

Since $\Delta_O = 10\Delta_G$, (A1) can also be written as

$$\begin{aligned} Y_G^*(w) = \sum_{n=-20}^{20} B_{Ow}(10n\Delta_G) \sum_{k=-70}^{70} B_{G(w+10n\Delta_G)}(k\Delta_G) \\ \times X(w + (10n + k)\Delta_G). \end{aligned} \tag{A2}$$

It can be further written as

$$Y_G^*(w) = \sum_{m=-270}^{270} B_{Gw}^*(m\Delta_G) X(w + m\Delta_G) \tag{A3}$$

where B_{Gw}^* represents convolved GOME-2 SRF with OMPS NM SRF for wavelength w. It can be written as

$$B_{Gw}^*(m\Delta_G) = \sum_{n=-20}^{20} B_{Ow}(10n\Delta_G) \sum_{k=-70}^{70} B_{G(w+10n\Delta_G)}(k\Delta_G) \tag{A4}$$

where integers n, k, m in (A3) and (A4) satisfy $10n + k = m$.

B^*_{Gw} covers ±2.7 nm from the center wavelength with sampling interval equal to the smaller sampling interval of the two sensors, that is, 0.01 nm.

Therefore, the convolution errors of radiance or solar irradiance at wavelength w, $\Delta\text{Rad}_{\text{CE}}$, can be written as from the difference between (A3) and (1B)

$$\begin{aligned}\Delta\text{Rad}_{\text{CE}} &= Y^*_G(w) - Y_O(w) \\ &= \sum_{m=-270}^{270} B^*_{Gw}(m\Delta_G)X(w+m\Delta_G) \\ &\quad - \sum_{n=-20}^{20} B_{Ow}(n\Delta_O)X(w+n\Delta_O). \end{aligned} \tag{A5}$$

Relative convolution errors of radiance or solar irradiance at wavelength w can be written as:

$$\begin{aligned}\delta_X(w) &= 1 - \frac{Y_O(w)}{Y^*_G(w)} \\ &= 1 - \frac{\sum_{n=-20}^{20} B_{Ow}(n\Delta_O)X(w+n\Delta_O)}{\sum_{m=-270}^{270} B^*_{Gw}(m\Delta_G)X(w+m\Delta_G)} \end{aligned} \tag{A6}$$

where Y represents radiance or solar irradiance, and X represents monochromatic radiance or solar irradiance illumination.

Equation (A7) is relative convolution errors of reflectance to convolved GOME-2 measurements at wavelength w

$$\begin{aligned}&\delta_R(w) \\ &\quad = 1 - \frac{\text{Ref}_O(w)}{\text{Ref}^*_G(w)} = 1 - \frac{\frac{\sum_{n=-20}^{20} B_{Ow}(n\Delta_O)R(w+n\Delta_O)}{\sum_{n=-20}^{20} B_{Ow}(n\Delta_O)I(w+n\Delta_O)}}{\frac{\sum_{m=-270}^{270} B^*_{Gw}(m\Delta_G)R(w+m\Delta_G)}{\sum_{m=-270}^{270} B^*_{Gw}(m\Delta_G)I(w+m\Delta_G)}}. \end{aligned} \tag{A7}$$

Appendix B
Convolution Error Calculation Formula Derivation for More General Cases

Equations (A3) and (A4) can be modified to apply to more general cases. Assume that instrument A has narrow bandwidth, the number of weights in its discrete SRF is $2R_A + 1$, and the sampling interval is Δ_A. Instrument B has a wider bandwidth, the number of weights in its discrete SRF is $2R_B + 1$, the sampling interval is $\Delta_B.\Delta_B = l\Delta_A$, and l is an integer. Then, convolved instrument A radiance can also be written as

$$\begin{aligned}Y^*_A(w) &= \sum_{n=-R_B}^{R_B} B_{Bw}(\ln\Delta_A) \sum_{k=-R_A}^{R_A} B_{A(w+\ln\Delta_A)}(k\Delta_A) \\ &\quad \times X(w+(\ln+k)\Delta_A) \\ &= \sum_{m=-(lR_B+R_A)}^{lR_B+R_A} B^*_{Aw}(m\Delta_A)X(w+m\Delta_A) \end{aligned} \tag{B1}$$

where B_{Bw} and B_{Aw} are normalized discrete SRF for instruments B and A, respectively. B^*_{Aw} represents convolved instrument A's SRF with B's SRF for wavelength w. It can be calculated by

$$B^*_{Aw}(m\Delta_A) = \sum_{n=-R_B}^{R_B} B_{Bw}(\ln\Delta_A) \sum_{k=-R_A}^{R_A} B_{A(w+\ln\Delta_A)}(k\Delta_A) \tag{B2}$$

where integers $l, n, k,$ and m in the above equation satisfy $\ln + k = m$.

If $\Delta_B = l\Delta_A$, and l is not an integer, then the following steps can be used to find convolved instrument A's measurements.

Step 1: Find a sampling interval Δ_C that satisfies: $\Delta_A > \Delta_C$, $\Delta_B = j\Delta_C$. j is an integer

Step 2: Interpolate instrument A's original discrete SRF with sampling interval equals Δ_A to a new discrete SRF with sampling interval equals Δ_C and then normalize it. B_{Cw} represents the new normalized discrete SRF. Number of weights of B_{Cw} is $2R_C+1$.

Step 3: Convolved instrument A's measurements with B's SRF can be written as

$$\begin{aligned}Y^*_A(w) &= \sum_{n=-R_B}^{R_B} B_{Bw}(jn\Delta_C) \sum_{k=-R_C}^{R_C} B_{C(w+jn\Delta_C)} \\ &\quad \times (k\Delta_C)X(w+(jn+k)\Delta_C) \\ &= \sum_{m=-(jR_B+R_C)}^{jR_B+R_C} B^*_{Cw}(m\Delta_C)X(w+m\Delta_C) \end{aligned} \tag{B3}$$

where B^*_{Cw} represents convolved instrument A's new normalized SRF for wavelength w. It can be calculated by

$$\begin{aligned}B^*_{Cw}(m\Delta_A) = \sum_{n=-R_B}^{R_B} B_{Bw}(jn\Delta_C) \sum_{k=-R_C}^{R_C} B_{C(w+jn\Delta_C)} \\ \times (k\Delta_C) \end{aligned} \tag{B4}$$

where integers $j, n, k,$ and m in the above equation satisfy $jn + k = m$.

Acknowledgment

The authors would like to thank Trevor Beck for valuable information on units in GOME-2 L1B data.

Disclaimer

The scientific results and conclusions, as well as any views or opinions expressed herein, are those of the author(s) and do not necessarily reflect those of NOAA or the Department of Commerce.

References

[1] D. C. Tobin, H. E. Revercomb, C. C. Moeller, and T. S. Pagano, "Use of atmospheric infrared sounder high–spectral resolution spectra to assess the calibration of Moderate resolution Imaging Spectroradiometer on EOS Aqua," *J. Geophys. Res.*, vol. 111, no. D9, 2006, Art. no. D09S05.

[2] L. Wang, C. Cao, and P. Ciren, "Assessing NOAA-16 HIRS radiance accuracy using simultaneous nadir overpass observations from AIRS," *J. Atmos. Ocean. Technol.*, vol. 24, no. 9, pp. 1546–1561, Sep. 2007.

[3] L. Wang *et al.*, "Consistency assessment of atmospheric infrared sounder and infrared atmospheric sounding interferometer radiances: Double differences versus simultaneous nadir overpasses," *J. Geophys. Res.*, vol. 116, no. D11, 2011, Art. no. D11111.

[4] X. Wu *et al.*, "Evaluation of the sensor data record from the nadir instruments of the ozone mapping profiler suite (OMPS)," *J. Geophys. Res., Atmos.*, vol. 119, no. 10, pp. 6170–6180, May 2014.

[5] W. Wu *et al.*, "An accurate method for correcting spectral convolution errors in intercalibration of broadband and hyperspectral sensors," *J. Geophys. Res., Atmos.*, vol. 123, no. 17, pp. 9238–9255, Sep. 2018.

[6] D. Liang, B. Yan, N. Sun, L. Flynn, C. Pan, and T. Beck, "Lifetime performance assessment of SNPP OMPS nadir MAPPER SDR data using simultaneous nadir overpass collocated observations with Gome-2," in *Proc. IEEE Int. Geosci. Remote Sens. Symp. (IGARSS)*, Sep. 2020, pp. 6258–6261, doi: 10.1109/IGARSS39084.2020.9324566.
[7] C. Cao and A. K. Heidinger, "Inter-comparison of the longwave infrared channels of MODIS and AVHRR/NOAA-16 using simultaneous nadir observations at orbit intersections," *Proc. SPIE*, vol. 4814, Sep. 2002, pp. 306–316.
[8] C. Pan, F. Weng, T. Beack, L. Flynn, and S. Ding, "Recent improvements to Suomi NPP ozone mapper profiler suite nadir mapper sensor data records," *IEEE Trans. Geosci. Remote Sens.*, vol. 55, no. 10, pp. 5770–5776, Oct. 2017, doi: 10.1109/TGRS.2017.2714103.
[9] L. Flynn *et al.*, "Performance of the ozone mapping and profiler suite (OMPS) products," *J. Geophys. Res., Atmos.*, vol. 119, no. 10, pp. 6181–6195, May 2014.
[10] J. V. Rodriguez, C. J. Seftor, C. G. Wellemeyer, and K. Chance, "An overview of the nadir sensor and algorithms for the NPOESS ozone mapping and profiler suite (OMPS)," *Proc. SPIE*, vol. 4891, pp. 65–75, Apr. 2003.
[11] R. Munro *et al.*, "The GOME-2 instrument on the Metop series of satellites: Instrument design, calibration, and level 1 data processing—An overview," *Atmos. Meas. Techn.*, vol. 9, no. 3, pp. 1279–1301, Mar. 2016.
[12] C. Cao, M. Weinreb, and H. Xu, "Predicting simultaneous nadir overpasses among polar-orbiting meteorological satellites for the intersatellite calibration of radiometers," *J. Atmos. Ocean. Technol.*, vol. 21, no. 4, pp. 537–542, Apr. 2004.
[13] C. Cao, M. D. Goldberg, F. Wen, C.-Z. Zou, and P. Ciren, "Simultaneous nadir overpasses for NOAA-6 to NOAA-17 satellites from 1980 to 2003 for the inter-satellite calibration of radiometers," Nat. Ocean. Atmos. Admin., Washington, DC, USA, Tech. Rep. 118, 2005.
[14] S. Uprety, C. Cao, X. Xiong, S. Blonski, A. Wu, and X. Shao, "Radiometric intercomparison between Suomi-NPP VIIRS and Aqua MODIS reflective solar bands using simultaneous nadir overpass in the low latitudes," *J. Atmos. Ocean. Technol.*, vol. 30, no. 12, pp. 2720–2736, Dec. 2013.
[15] C. Cao, S. Uprety, and S. Blonski, "Establishing radiometric consistency among VIIRS, MODIS, and AVHRR using SNO and SNOx methods," in *Proc. IEEE Int. Geosci. Remote Sens. Symp.*, Jul. 2012, pp. 6928–6931, doi: 10.1109/IGARSS.2012.6352569.
[16] C.-Z. Zou *et al.*, "Recalibration of microwave sounding unit for climate studies using simultaneous nadir overpasses," *J. Geophys. Res.*, vol. 111, no. D19, 2006, Art. no. D19114.
[17] A. V. Oppenheim, *Signal and Systems*. London, U.K.: Pearson, 1996.
[18] T. F. Eck, P. K. Bhartia, and J. B. Kerr, "Satellite estimation of spectral UVB irradiance using TOMS derived total ozone and UV reflectivity," *Geophys. Res. Lett.*, vol. 22, no. 5, pp. 611–614, Mar. 1995.
[19] Z. Cai *et al.*, "Characterization and correction of Global Ozone Monitoring Experiment 2 ultraviolet measurements and application to ozone profile retrievals," *J. Geophys. Res., Atmos.*, vol. 117, no. D7, Apr. 2012, Art. no. D07305.
[20] "Metop-B GOME annual in-flight performance report 2014," EUMETSAT, Darmstadt, Germany, Tech. Rep., EUM/OPS/EPS/REP/14/771772, v2A, 2015.
[21] C. Pan and L. Flynn, "Solar observation of ozone mapping and profiler suite nadir system during the first 3 years of on-orbit operation," *J. Appl. Remote Sens.*, vol. 9, no. 1, Aug. 2015, Art. no. 094095.

Ding Liang received the B.S.E.E. degree in electronics and information system from Wuhan University, Wuhan, China, in 2002, the M.S.E.E. and Ph.D. degrees in electrical engineering from the University of Washington, Seattle, WA, USA, in 2008 and 2009, respectively.

From 2005 to 2009, she was a Research Assistant with the Department of Electrical Engineering, University of Washington, where she was involved in theoretical modeling and numerical simulation of electromagnetic wave propagation and scattering in random media with application to passive and active microwave remote sensing of terrestrial snow and rough surface. Since 2009, she has been focusing on satellite calibration and validation algorithm development, satellite performance monitoring and evaluation with the Center for Satellite Applications and Research (STAR), National Oceanic and Atmospheric Administration (NOAA), College Park, MD, USA.

Banghua Yan received the Ph.D. degree in atmospheric physics from the Institute of Atmospheric Physics, Chinese Academy of Sciences, Beijing, China, in 1997, and the Ph.D. degree in atmospheric radiation from the University of Alaska, Fairbanks, AK, USA, in 2001.

She is currently a Physical Scientist with the Satellite Calibration and Data Assimilation Branch, NOAA Center for Satellite Applications and Research (STAR). From 1999 to 2010, she worked for the STAR through companies or NOAA Joint Center for Satellite Data Assimilation (JCSDA) or the Earth System Science Interdisciplinary Center, University of Maryland, College Park, MD, USA. During this period, she significantly contributed to the developments of microwave land, snow, and sea ice emissivity models, and microwave satellite instrument data assimilation studies. Those work have significantly improved the use of satellite sounding data in numerical weather prediction (NWP) models. The land, snow, and sea ice microwave emissivity models have been implemented into the NOAA NCEP NWP model and the JCSDA community radiative transfer model that has been successfully used in several operational data assimilation systems in the U.S. From 2010 to 2017, she was an Oceanographer with the NOAA Office of Satellite Data Processing and Distribution, Camp Springs, MD, USA, to lead the NOAA operational ocean color production system. In addition, from 2017 to 2019, she successfully led calibrations/validations of Metop-C Advanced Microwave Sounding Unit-A (AMSU-A) to ensure the operation of AMSU-A data. She also coordinated the JPSS/STAR (JSTAR) mission program for more than half years. She currently leads calibrations/validations of Joint Polar Satellite System Ozone Mapping and Profiler Suite (OMPS) and the STAR integrated calibration/validation system (ICVS) long-term monitoring. She has published more than 30 articles in international peer-reviewed journals as the first or co-author.

Lawrence Flynn received the Ph.D. degree in applied mathematics from the University of California at Davis, Davis, CA, USA, in 1987.

He joined NOAA/NESDIS, Washington, DC, USA, in 1996 and has been a Research Scientist for the last 25 years. His duties include research and analysis for validation, algorithm development, and calibration of existing and next generation satellite-based ozone sensors.